

## CERAMICS

# Double-negative-index ceramic aerogels for thermal superinsulation

Xiang Xu<sup>1,2\*</sup>, Qiangqiang Zhang<sup>3\*</sup>, Menglong Hao<sup>4,5\*</sup>, Yuan Hu<sup>6</sup>, Zhaoyang Lin<sup>1</sup>, Lele Peng<sup>1</sup>, Tao Wang<sup>1</sup>, Xuexin Ren<sup>4</sup>, Chen Wang<sup>7</sup>, Zipeng Zhao<sup>7</sup>, Chengzhang Wan<sup>1</sup>, Huilong Fei<sup>1</sup>, Lei Wang<sup>8</sup>, Jian Zhu<sup>8</sup>, Hongtao Sun<sup>1,9</sup>, Wenli Chen<sup>2</sup>, Tao Du<sup>2</sup>, Biwei Deng<sup>10</sup>, Gary J. Cheng<sup>10</sup>, Imran Shakir<sup>11</sup>, Chris Dames<sup>4,12</sup>, Timothy S. Fisher<sup>6</sup>, Xiang Zhang<sup>4</sup>, Hui Li<sup>2†</sup>, Yu Huang<sup>7†</sup>, Xiangfeng Duan<sup>1†</sup>

Ceramic aerogels are attractive for thermal insulation but plagued by poor mechanical stability and degradation under thermal shock. In this study, we designed and synthesized hyperbolic architected ceramic aerogels with nanolayered double-pane walls with a negative Poisson's ratio ( $-0.25$ ) and a negative linear thermal expansion coefficient ( $-1.8 \times 10^{-6}$  per °C). Our aerogels display robust mechanical and thermal stability and feature ultralow densities down to  $\sim 0.1$  milligram per cubic centimeter, superelasticity up to 95%, and near-zero strength loss after sharp thermal shocks ( $275^\circ\text{C}$  per second) or intense thermal stress at  $1400^\circ\text{C}$ , as well as ultralow thermal conductivity in vacuum [ $\sim 2.4$  milliwatts per meter-kelvin (mW/m·K)] and in air ( $\sim 20$  mW/m·K). This robust material system is ideal for thermal superinsulation under extreme conditions, such as those encountered by spacecraft.

**T**hermal insulation under extreme conditions, such as rapid temperature changes and long-term high-temperature exposure in aerospace and thermal power fields, requires exceptional stability and reliability for personal and property protection (1–3). Because of their low density, low thermal conductivity, and excellent fire and corrosion resistance (4, 5), ceramic aerogels are attractive candidates for thermal insulation. However, owing to their brittle nature and crystallization-induced pulverization behavior (6), ceramic aerogels often suffer from serious strength degradation and structural

collapse under large thermal gradients or extended high-temperature exposure. Examples of degradation that may result in catastrophic failure include structural cracks in silica aerogels (7), strength degradation for SiC aerogels (8), and volume shrinkage for alumina aerogels (9). Therefore, robust mechanical and thermal stability are the key roadblocks to using ceramic aerogels for reliable thermal insulation under extreme conditions.

Prior efforts to improve thermal stability primarily focused on overcoming brittleness by making flexible amorphous one-dimensional (1D) fibrous structures. Fiber-reinforced SiO<sub>2</sub> aerogels (10), SiO<sub>2</sub> nanofibrous aerogels (11, 12), SiC nanowire aerogels (8), alumina nanolattices (13), oxide ceramic (TiO<sub>2</sub>, ZrO<sub>2</sub>, and BaTiO<sub>3</sub>) nanofiber sponges (14), and BN fibrous aerogels (15) have been developed with large, recoverable deformability (up to 80% compressive strain) derived from the elastic fibrous structures. However, owing to the large thermal expansion and pulverization behaviors of these ceramic materials and the weak point-linking pattern between 1D fibers, such fibrous ceramic aerogels still suffer from structural degradation under rapid thermal shocks or high temperatures. Moreover, the 1D fibrous building blocks lead to interconnected macroscale pores that cannot effectively mitigate solid conduction or convection in air. As a result, the thermal conductivities of fibrous ceramic aerogels are typically higher than that of stationary air [24 milliwatts per meter-kelvin (mW/m·K)] (8–15).

In contrast, aerogels constructed from 2D nanosheets, such as graphene aerogels (16), feature durable face-to-face stacking interactions between 2D nanosheets to endow ultralarge deformability with up to 99% compression strain

(17, 18). Additionally, the face-to-face stacking between the 2D sheets also partitions the 3D aerogels into nearly isolated cells to effectively reduce the air conduction and convection, producing ultralow thermal conductivities below stationary air (19, 20). However, because of their easy oxidation and flammability, graphene aerogels are generally not stable in air at high temperatures ( $>500^\circ\text{C}$ ). Porous ceramic structures synthesized by direct chemical reaction (21), elemental substitution (22), and template-assisted methods (23, 24) have attracted considerable interest, including template-assisted methods that produce 3D frameworks to replicate the template architecture. However, volume shrinkage and strength degradation of the resulting ceramic aerogels, which may be attributed to poor cross-linking between ceramic blocks and limited deformability of the typical templates, remain problematic (9, 11, 15, 23).

Materials with negative-index properties derived from specifically designed structures can substantially enhance performance metrics and allow for the development of distinctive attributes (25, 26). Mechanical metamaterials with a negative Poisson's ratio (NPR) have attracted considerable attention for their unusual mechanical enhancement for diverse applications, particularly in stringent environments such as aerospace and defense (27). By rationally manipulating the structure, materials with a NPR can deliver superior deformability and fracture toughness for overcoming the brittle nature of ceramic aerogels. Simultaneously engineering other negative indexes (28–32) may synergistically enhance additional physical properties, such as thermal stability.

Here, we report the design of a ceramic material with robust mechanical and thermal stability under extreme conditions. The ceramic has a double-paned metastructure with a NPR and a negative thermal expansion coefficient (NTEC). We used specially designed 3D graphene aerogel templates to synthesize hexagonal boron nitride aerogels (hBNAGs) and  $\beta$  silicon carbide aerogels ( $\beta$ SiCAGs) with excellent thermal and mechanical stabilities. The resulting hBNAGs exhibited ultralow density ( $\sim 0.1$  mg/cm<sup>3</sup>), superelasticity (up to 95%), thermal superinsulation ( $\sim 2.4$  mW/m·K in vacuum and  $\sim 20$  mW/m·K in air), and thermal stability under sharp thermal shocks ( $\sim 275^\circ\text{C/s}$ ) and long-term high-temperature exposures ( $900^\circ\text{C}$  in air and  $1400^\circ\text{C}$  in vacuum).

We designed a hierarchical porous structure with hyperbolic architecture to obtain a NPR (Fig. 1A). The subcells were designed with double-pane walls to reduce the wall thickness without compromising the mechanical strength and facilitate the out-of-plane vibration modes for NTEC (11, 13, 17). This metastructure design ensures widely distributed compressive strain under mechanical or thermal excitations (33) (fig. S1). To obtain the designed structure characteristics, we first produced the graphene aerogel templates using a modified hydrothermal reduction (MHR) and noncontact freeze drying (NCFD) technique (17, 18) and then prepared hBNAGs or  $\beta$ SiCAGs through a template-assisted

<sup>1</sup>Department of Chemistry and Biochemistry, University of California, Los Angeles, CA 90095, USA. <sup>2</sup>Key Lab of Structures Dynamic Behavior and Control of the Ministry of Education, Harbin Institute of Technology, Harbin 150090, P. R. China. <sup>3</sup>College of Civil Engineering and Mechanics, Key Laboratory of Mechanics on Disaster and Environment in Western China, Lanzhou University, Lanzhou 730000, P. R. China. <sup>4</sup>Department of Mechanical Engineering, University of California, Berkeley, CA 94720, USA. <sup>5</sup>Key Laboratory of Energy Thermal Conversion and Control of Ministry of Education, School of Energy and Environment, Southeast University, Nanjing 210096, P. R. China. <sup>6</sup>Department of Mechanical and Aerospace Engineering and California NanoSystems Institute, University of California, Los Angeles, CA 90095, USA. <sup>7</sup>Department of Materials Science and Engineering, University of California, Los Angeles, CA 90095, USA. <sup>8</sup>State Key Laboratory for Chemo/Biosensing and Chemometrics, College of Chemistry and Chemical Engineering, Hunan University, Changsha 410082, P. R. China. <sup>9</sup>Department of Mechanical and Industrial Engineering, New Jersey Institute of Technology, Newark, NJ 07102, USA. <sup>10</sup>School of Industrial Engineering, Purdue University, West Lafayette, IN 47907, USA. <sup>11</sup>Sustainable Energy Technologies Centre, College of Engineering, King Saud University, Riyadh, Kingdom of Saudi Arabia. <sup>12</sup>Materials Sciences Division, Lawrence Berkeley National Laboratory, Berkeley, CA 94720, USA.

\*These authors contributed equally to this work.

†Corresponding author. Email: xduan@chem.ucla.edu (X.D.); yhuang@seas.ucla.edu (Y.H.); lihui@hit.edu.cn (H.L.)

chemical vapor deposition (CVD) process (Fig. 1B and figs. S2 to S4). For simplicity, we focus our discussion on hBNAGs. The resulting hBNAGs exhibit ultralow densities of less than  $10 \text{ mg/cm}^3$  (17), with a lowest density of  $0.1 \text{ mg/cm}^3$ , establishing them as a member of the group of superlight solid materials (3, 8, 11, 34–36) (Fig. 2, A and B, and fig. S5). We attribute the ultralow density of  $0.1 \text{ mg/cm}^3$  to the highly porous structure with atomically thin cell walls (fig. S6).

We characterized the chemical composition and crystallinity of hBNAGs using x-ray photoelectron spectroscopy, Raman spectra, and x-ray diffraction (XRD) (fig. S7). The results from these characterizations reveal the high-crystallinity nature of hBN in the aerogel framework. In particular, the characteristic Raman and XRD peaks for hBN gradually narrow with increasing intensity on annealing at higher temperature, suggesting a systematic structural evolution from amorphous to polycrystalline BN. We also performed detailed structural characterizations of  $\beta\text{SiCAGs}$  (figs. S8 and S9). We investigated the morphology and structure of hBNAGs by scanning electron microscopy (SEM), Brunauer-Emmett-Teller measurement, spherical aberration-corrected transmission electron microscopy (TEM), and atomic force microscopy (AFM). The microstructure of the hBNAGs remained essentially the same as that of the graphene aerogel templates

(Fig. 2C and fig. S10), with the same facial-linking pattern between cell walls (fig. S11, and  $\beta\text{SiCAGs}$  in fig. S12). Thermal etching of graphene templates allowed formation of double-pane wall structures (Fig. 2D). The high bending stiffness of hBN prevented face-to-face collapse (37). We could tune the average gap size between the double-pane walls from a few to tens of nanometers (Fig. 2D and fig. S13) by controlling the wall thickness of graphene templates (17). The hBNAGs exhibited an ultrahigh porosity (99.99%) and a larger specific surface area ( $1080 \text{ m}^2/\text{g}$ ) (fig. S14) than those reported for other ultralight materials ( $\sim 800 \text{ m}^2/\text{g}$  for silica or carbon aerogels) (4, 16). The cell walls were made of highly crystalline hBN from planar-view TEM and selected-area electron diffraction studies (fig. S15). The cell walls consist of single or multi-layer well-ordered hBN with clearly resolved interlayer spacing of  $0.33 \text{ nm}$  (fig. S15), which we confirmed with AFM imaging (fig. S16). The wall thickness varied from 1 to  $100 \text{ nm}$ , depending on the precursor concentration in the CVD chamber.

We investigated the mechanical properties of the hBNAGs with uniaxial quasi-static compression (Fig. 3). We compressed the sample from 10 to  $0.5 \text{ mm}$ , a strain of 95%, and recovered the original configuration after pressure release (Fig.

3A and movie S1). The recoverable strain is higher than previously reported values for ceramic aerogels, which top out at 80% (8, 11–15, 38). We then demonstrated that the hBNAG sample can be repeatedly compressed at 90% strain for >100 cycles with little structural degradation (fig. S17 and movie S2). The Young's modulus is as high as  $25 \text{ kPa}$  for the first cycle with a slightly shrinking hysteresis loop during the next 20 cycles. The loop remains nearly unchanged up to the 100th cycle. The aerogel height remains nearly the same as the original value (residual strain < 4%), and the ultimate stress and Young's modulus gradually reach their equilibrium states with total decreases of 10 and 18%, respectively (Fig. 3B). We found similar superelastic behavior (strain up to 95%) in  $\beta\text{SiCAGs}$  (fig. S18), indicating that the templating method should be a general one for making elastic ceramics. Together, our aerogels show attractive mechanical properties when compared with ceramic aerogels with 1D fibrous structures (Fig. 3C) (8, 11–15, 38). For hBNAGs, the maximum strain is 95% compared with 80% for  $\text{SiO}_2$  aerogels, the ultimate stress is up to  $0.14 \text{ MPa}$  compared with  $0.03 \text{ MPa}$  for  $\text{Al}_2\text{O}_3$  aerogels, and the strength loss is 10% at  $\epsilon_{100} = 90\%$  compared with 40% at  $\epsilon = 50\%$  in amorphous BN aerogels.

Next, we investigated the dependence of the hBNAG deformation on the microscale wall

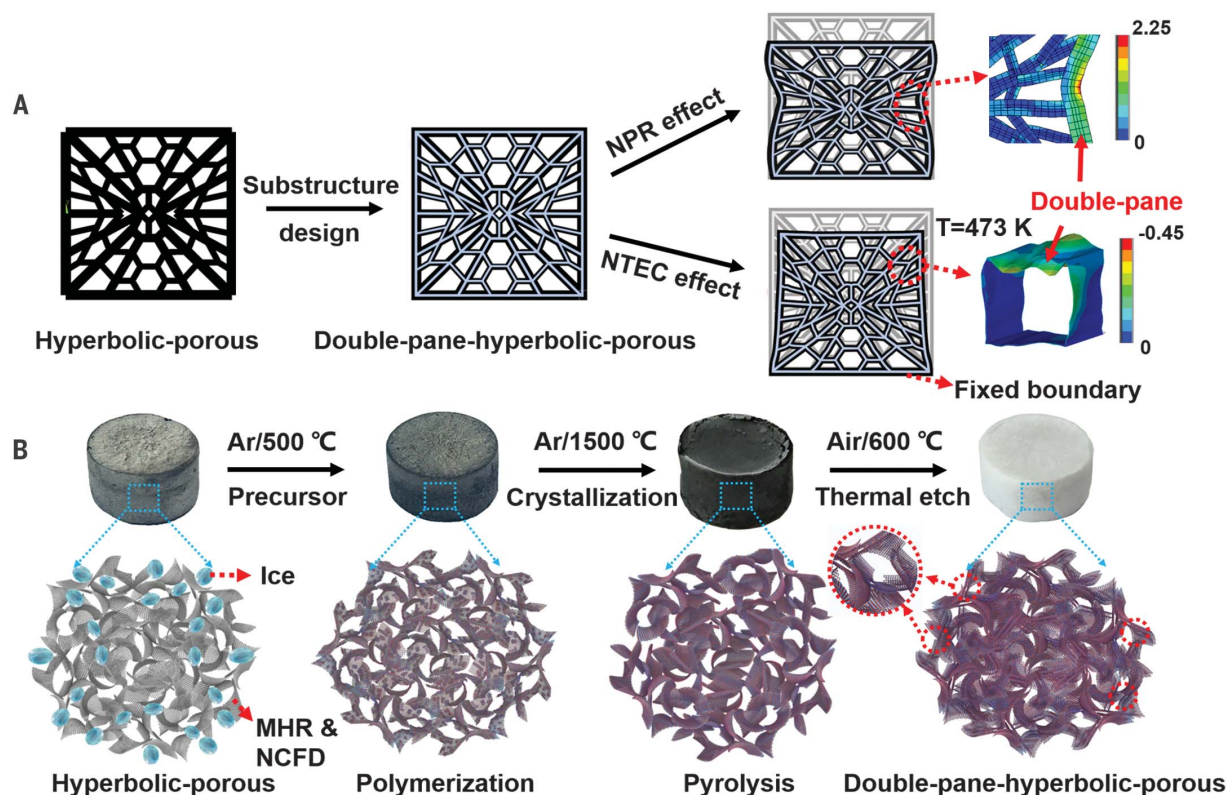


**Fig. 1. Structure design and fabrication of the ceramic aerogel meta-material.** (A) Illustration of the metastructure design of ceramic aerogels. The units of the colored scale bars are as follows: kilopascals for NPR and percentage (with strain zoomed by 30 times) for NTEC. (B) Illustration

of the CVD synthesis process of the double-paned hyperbolic ceramic aerogels. The NCFD technique is used to render hyperbolic structure in graphene aerogel templates by manipulating the ice crystal growth direction (17, 18).

thickness (Fig. 3D and fig. S19) and macroscale morphology to optimize the mechanical robustness of hBNAGs. The resilience of the walls determines their elastic behavior and depends on their thickness. Thin walls (<10 nm) have highly elastic (40

to 90% strain) behaviors due to their limited resilience. Increased wall thickness (up to 40 nm) changes the deformability to superelastic (90 to 95% strain). Further increasing the wall thickness (>60 nm) results in brittleness similar to other

bulk ceramic materials and a drop in ductility of 10% due to the confined bending deformation. Our observations are consistent with our molecular dynamics (MD) simulations (fig. S20) (33). A different way to look at this behavior is by plotting the relative Young's modulus ( $E/E_s$ ) versus the relative density ( $\rho/\rho_s$ ) as it scaled linearly as  $E/E_s \sim (\rho/\rho_s)^{1.54}$  (Fig. 3E). This scaling corresponds well with the flexibility of hBNAGs within wall thicknesses of 1 to 40 nm. Samples with larger wall thickness (>100 nm) exhibit a larger  $E/E_s \sim (\rho/\rho_s)$  trend of >2, which is similar to most existing rigid and brittle inorganic porous monoliths (11).

The theoretical structure design (fig. S1) and our previous studies (17, 18) show the mechanical benefits of having graphene aerogels with a NPR instead of positive or zero Poisson's ratios. The hyperbolic-patterned macrostructure facilitates the bending Poisson's effect (39) and triggers the oriented out-of-plane buckling of the cell walls and widely distributes compressive strain during the uniaxial compression of the samples (Fig. 3F, figs. S21 and S22, and movie S3). We demonstrated this with in situ SEM observations and analysis of strain mapping (fig. S23) (17, 33).

Thermally excited ripples could induce negative thermal expansion behavior in 2D nanolayered structures (40). Our double-pane structure design for the porous framework cell walls reduces the wall thickness for lower out-of-plane stiffness and releases by an additional degree of freedom to facilitate the out-of-plane vibration modes (11, 13, 17), leading to the contractions of the cell

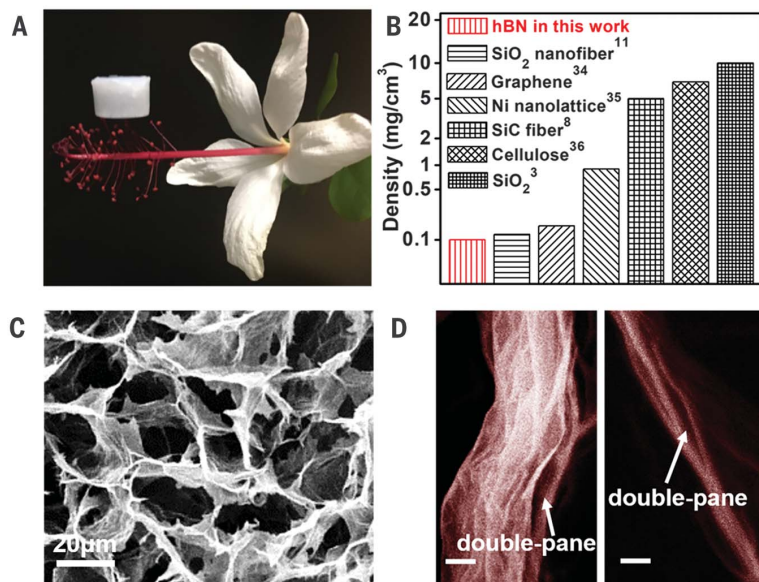


**Fig. 2. Material characterization of hBNAGs.** (A) An optical image showing an hBNAG sample resting on the stamen of a flower. All tests were done on ceramic aerogels with a density of 5 mg/cm<sup>3</sup> unless otherwise noted. (B) The lightest hBNAG sample compared with other ultralight materials. The superscripted numbers indicate the corresponding referenced work. (C) SEM image of hBNAG. (D) SEM images of the double-pane wall structure of hBNAGs. Scale bars, 20 nm.

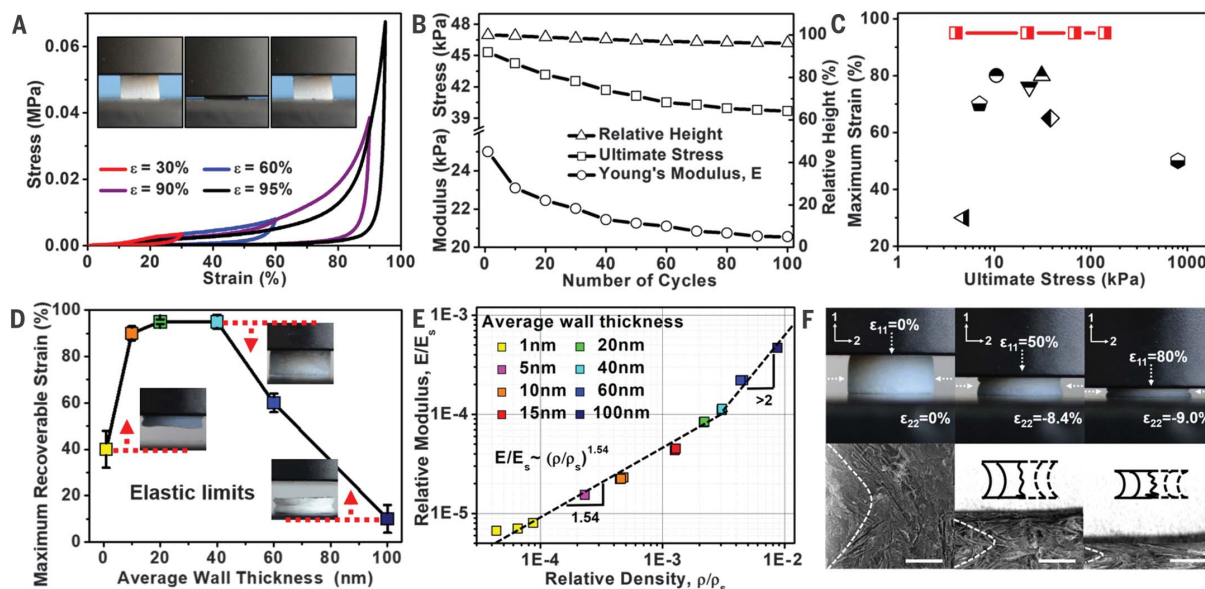


**Fig. 3. Mechanical properties of hBNAGs.** (A) Uniaxial compression of hBNAGs with repeatable strain ( $\epsilon$ ) up to 95%. (Inset) Experimental snapshots of one compression cycle. (B) The ultimate stress, Young's modulus, and relative height for 100 compression cycles. (C) The maximum strain and ultimate stress of the hBNAGs compared with other ceramic aerogels. Red square, hBN in this work; circle, SiO<sub>2</sub> with binder (12); right-side-up triangle, SiO<sub>2</sub> fiber (11); upside-down triangle, SiC fiber (8); pentagon, BN sheet (15); diamond, Al<sub>2</sub>O<sub>3</sub> particle (38); hexagon, Al<sub>2</sub>O<sub>3</sub> lattice

(13); sideways triangle, oxide ceramic fiber (14). (D) The maximum elastic deformability of hBNAGs as a function of the wall thickness. (Inset) Morphologies of hBNAGs with different wall thicknesses beyond their maximum elastic strains. (E) The relative modulus (defined as their measured Young's modulus,  $E$ , divided by the Young's modulus of the constituent bulk solid,  $E_s$ ) of hBNAGs at relative densities. (F) Experimental snapshots of cross-sectional views and the corresponding SEM images of NPR behavior of the hBNAGs under uniaxial compression. Scale bars, 1 mm.

walls in the frameworks. Meanwhile, the highly porous frameworks provide sufficient deformation space for these thermally excited ripples, and the double-pane structures further reduce the reciprocal constraints between adjacent cell walls. As a result, we realized a framework structure with NTEC [as shown in MD and finite element (FE) analysis in figs. S1, S24, and S25] (33). A SEM image (fig. S26) of the cell walls of hBNAGs suspended on a Cu grid shows small ripples at room temperature, which are likely formed during the deposition process. After annealing at 800°C and cooling, these small ripples evolved into larger ones (a large alteration in the ripple geometry, with apparently larger amplitudes and longer wavelengths), indicating the slack of the sample due to the TEC mismatch between the substrate and sample. This behavior was similar to what we observed in our previous work on graphene for the NTEC property (40). We measured the effective TEC of the hBNAGs (fig. S27); bulk hBN has a TEC of  $40.5 \times 10^{-6}/^{\circ}\text{C}$  in the *c* direction (41), whereas the hBNAGs present an obvious linear NTEC of  $-10.7 \times 10^{-6}/^{\circ}\text{C}$  below 80°C and  $-1.8 \times 10^{-6}/^{\circ}\text{C}$  at higher temperature.  $\beta$ SiCAGs also show linear NTEC behavior (fig. S28). Compared with the general tensile fracture induced by positive thermal expansion, the thermally excited compression stress in the NTEC case can be dissipated by the superelasticity of the hBNAGs, opening a pathway to enhanced thermal stability.

We further investigated the structural responses of hBNAGs under rapid thermal shocks. We designed a pneumatic thermal shock testing

system for the lightweight aerogel materials (fig. S29). By switching the pneumatic devices at the tube ends, we rapidly drove the ceramic aerogels back and forth between the fixed hot and cold sources. We swiftly heated the hBNAGs to 900°C and cooled to  $-198^{\circ}\text{C}$  with a frequency up to 0.1 Hz and temperature variation speed up to 275°C/s (fig. S30 and movie S4) (33). We studied the mechanical strength and structure variation after 500 thermal shock cycles (Fig. 4A). The porous structure retained its original morphology (Fig. 4A, inset), and ultimate stress and maximum strain remained essentially unchanged. This indicated excellent structural stability and resistance to drastic temperature variations. Our NTEC material endured larger temperature swings (up to 1100°C) than silica aerogels (<600°C) with even less strength degradation (~3%) (Fig. 4B and fig. S31) (33).

We also evaluated the effect of high-temperature stress and did not observe apparent weight loss below 900°C in air and 1500°C in Ar from the thermogravimetric analysis (fig. S32); the high crystallinity of the hBNAGs (fig. S7) prevented the weight loss. Above 900°C in air, we found oxidation-induced formation of  $\text{B}_2\text{O}_3$  layers, resulting in an increase in weight. We kept the hBNAGs at 1400°C for 1 week and found no strength or volume loss (fig. S33). In comparison, previous  $\text{SiO}_2$ ,  $\text{Al}_2\text{O}_3$ , and BN aerogels all degraded under long-term, high-temperature conditions (7–9, 23).

With excellent mechanical and thermal stability, the ultralight ceramic aerogels represent an attractive thermal insulation material family. In

particular, the distinctive double-pane pore structure suppresses air conduction and convection as well as reduces solid conduction contribution with its tortuous thermal pathway, leading to an ultralow thermal conductivity. For example, the resulting hBNAGs with a density of  $5 \text{ mg}/\text{cm}^3$  exhibit a thermal conductivity ( $\kappa$ ) of  $2.4 \text{ mW}/\text{m}\cdot\text{K}$  at room temperature in vacuum conditions (pressure:  $\sim 10^{-5}$  torr), which slightly increased to  $8.19 \text{ mW}/\text{m}\cdot\text{K}$  at 500°C owing to the increased thermal radiation (Fig. 4C, figs. S34 to S36, and table S1) (33). In vacuum, the apparent thermal conductivity ( $\kappa_{\text{total}}$ ) is the sum of radiation ( $\kappa_{\text{rad}}$ ) and solid conduction ( $\kappa_{\text{cond}}$ ) contributions. Taking advantage of the different temperature dependence of thermal radiation and conduction (33), we separated these two contributions and estimated  $\kappa_{\text{cond}}$  to be only  $0.4 \text{ mW}/\text{m}\cdot\text{K}$ , which is among the lowest for any freestanding material (2, 20, 33, 42, 43) (Fig. 4D and fig. S37). We ascribe this low matrix thermal conduction to three major factors, namely the ultralow density, the nanosized grains within the hBN sheets, and the double-pane wall structure. Density directly affects the actual conduction pathway and therefore  $\kappa_{\text{cond}}$ . However, because pristine multilayer hBN films have a high in-plane thermal conductivity around  $400 \text{ W}/\text{m}\cdot\text{K}$ , the low density ( $\sim 0.2\%$  volume fraction) alone cannot explain the low  $\kappa_{\text{cond}}$ . The in-plane thermal transport within each sheet in the hBNAGs is highly suppressed by phonon scattering at grain boundaries because of the small grain size (50 to 100 nm). For few-layer hBN, calculations indicate this effect can reduce  $\kappa_{\text{cond}}$  by as much as 99% from the

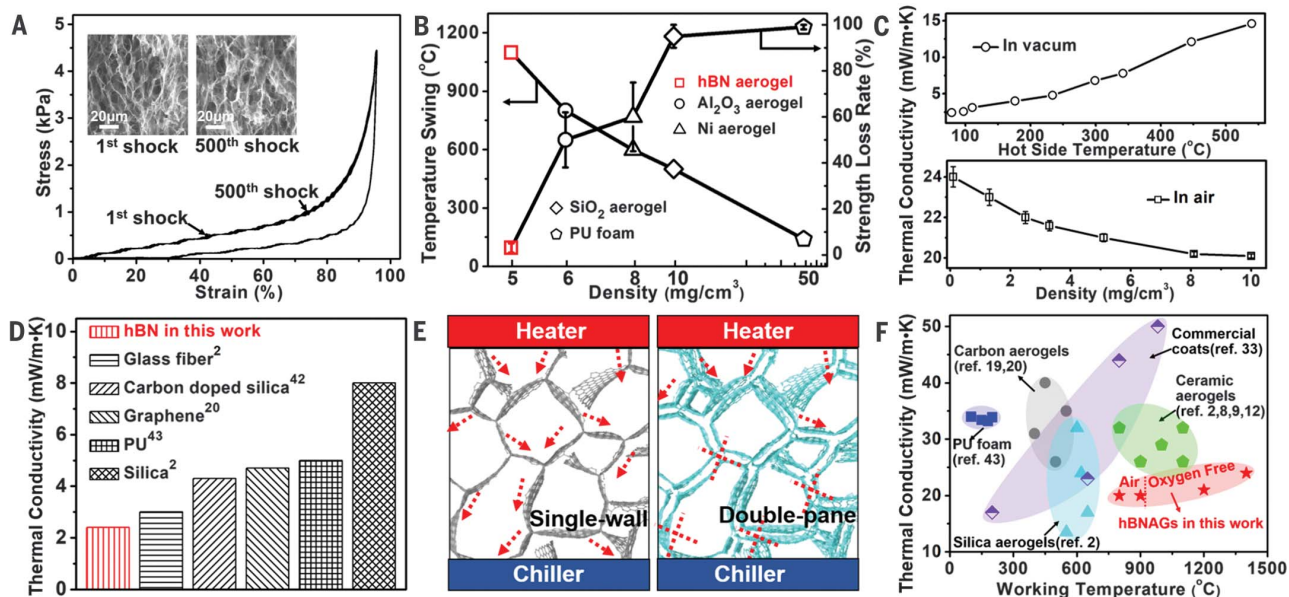


**Fig. 4. Thermal stability and thermal insulation properties of hBNAGs.**

(A) The strain and stress evolution after 500 cycles of sharp thermal shocks (275°C/s). (Inset) The SEM images of hBNAG frameworks after the first and last thermal shock tests. (B) The temperature differential and strength loss rate of hBNAGs for the thermal shocks compared with other aerogel-like materials. PU, polyurethane. (C) Thermal conductivity of hBNAGs in vacuum

(steady-state thermal measurement) and in air (transient thermal measurement). (D) The vacuum thermal conductivity of hBNAGs compared with other aerogel-like materials. The superscripted numbers indicate the corresponding referenced work. (E) The extra tortuous solid conduction path in double-paned hBNAGs. (F) Room temperature thermal conductivity in air versus working temperature for aerogel-like materials.

pristine value. Moreover, the interfaces connecting adjacent pores (Fig. 4E) create additional thermal resistance. For graphene aerogel with solid walls (19), this interface is a van der Waals bond, whereas for the hBNAGs with double-pane structure, because of the presence of the interface gap (~10 nm), heat transfer likely has to occur via near-field radiation (a much less effective process compared with van der Waals contact), thus substantially reducing  $\kappa_{\text{cond}}$  beyond the reach of conventional aerogels.

We also investigated the thermal conductivity at ambient conditions (Fig. 4C and figs. S38 to S41) (33). The hBNAGs with a density of ~0.1 mg/cm<sup>3</sup> exhibited  $\kappa$  of 24 mW/m·K, which is similar to that of stationary air. We increased the hBNAG density to 10 mg/cm<sup>3</sup>, and  $\kappa$  decreased gradually to ~20 mW/m·K owing to the decreased pore size and the nanosized double-pane structures in the cell walls (36, 38). This thermal superinsulating performance is better than that of stationary air. We placed a 20-mm-thick hBNAG directly on an alcohol flame (~500°C) and then put a fresh flower on top of the hBNAG (fig. S42). The top surface of the hBNAG maintained a relatively low temperature of about 45°C after being held on the flame for 15 min, and the flower exhibited only slight withering.

Ceramic aerogels thus present a combination of low thermal conductivity and robust thermal stability that offers considerable advantage for thermal superinsulation exposed to extreme conditions (e.g., high temperature or sharp thermal shocks) (Fig. 4F) (33) under which polymeric (43) and carbonaceous (19) insulating materials could easily collapse or ignite, and the traditional ceramic aerogels, such as SiO<sub>2</sub>, Al<sub>2</sub>O<sub>3</sub>, SiC, and BN (2, 4, 44), show poor mechanical stabilities.

## REFERENCES AND NOTES

- X. Q. Cao, R. Vassen, D. Stoeber, *J. Eur. Ceram. Soc.* **24**, 1–10 (2004).
- M. Koebel, A. Rigacci, P. Achard, *J. Solgel Sci. Techn.* **63**, 315–339 (2012).
- N. Bheekhun, A. R. Abu Talib, M. R. Hassan, *Adv. Mater. Sci. Eng.* **2013**, 406065 (2013).
- A. C. Pierre, G. M. Pajonk, *Chem. Rev.* **102**, 4243–4265 (2002).
- R. Baetens, B. P. Jelle, A. Gustavsen, *Energy Build.* **43**, 761–769 (2011).
- R. W. Cahn, *Nature* **332**, 112–113 (1988).
- A. Emmerling *et al.*, *J. Non-Cryst. Solids* **125**, 230–243 (1990).
- L. Su *et al.*, *ACS Nano* **12**, 3103–3111 (2018).
- G. Zu *et al.*, *Chem. Mater.* **25**, 4757–4764 (2013).
- D. Shi *et al.*, *Mater. Sci. Eng. A* **585**, 25–31 (2013).
- Y. Si, J. Yu, X. Tang, J. Ge, B. Ding, *Nat. Commun.* **5**, 5802 (2014).
- Y. Si, X. Wang, L. Dou, J. Yu, B. Ding, *Sci. Adv.* **4**, eaas8925 (2018).
- L. R. Meza, S. Das, J. R. Greer, *Science* **345**, 1322–1326 (2014).
- H. Wang *et al.*, *Sci. Adv.* **3**, e1603170 (2017).
- J. Yin, X. Li, J. Zhou, W. Guo, *Nano Lett.* **13**, 3232–3236 (2013).
- G. Gorgolis, C. Galiotis, *2D Mater.* **4**, 032001 (2017).
- X. Xu *et al.*, *Adv. Mater.* **28**, 9223–9230 (2016).
- Q. Zhang *et al.*, *Adv. Mater.* **28**, 2229–2237 (2016).
- Q. Zhang *et al.*, *ACS Appl. Mater. Interfaces* **9**, 14232–14241 (2017).
- Y. Xie *et al.*, *Carbon* **98**, 381–390 (2016).
- J. Li *et al.*, *Nanotechnology* **24**, 155603 (2013).
- M. Rousseas *et al.*, *ACS Nano* **7**, 8540–8546 (2013).
- Y. Song *et al.*, *Sci. Rep.* **5**, 10337 (2015).
- X. Zeng *et al.*, *Chem. Mater.* **27**, 5849–5855 (2015).
- N. Engheta, R. W. Ziolkowski, Eds., *Metamaterials: Physics and Engineering Explorations* (Wiley, 2006).
- T. J. Cui, D. R. Smith, R. P. Liu, Eds., *Metamaterials: Theory, Design, and Applications* (Springer, 2010).
- C. Huang, L. Chen, *Adv. Mater.* **28**, 8079–8096 (2016).
- R. H. Baughman, S. Stafström, C. Cui, S. O. Dantas, *Science* **279**, 1522–1524 (1998).
- A. L. Goodwin *et al.*, *Science* **319**, 794–797 (2008).
- R. Lakes, K. W. Wojciechowski, *Phys. Stat. Sol. B* **245**, 545–551 (2008).
- Y. Sun, N. Pugno, *Materials* **6**, 699–712 (2013).
- D. Mousanezhad *et al.*, *Sci. Rep.* **5**, 18306 (2015).
- Materials and methods are available as supplementary materials.
- H. Sun, Z. Xu, C. Gao, *Adv. Mater.* **25**, 2554–2560 (2013).
- T. A. Schaedler *et al.*, *Science* **334**, 962–965 (2011).
- B. Wicklein *et al.*, *Nat. Nanotechnol.* **10**, 277–283 (2015).
- A. E. Tanur *et al.*, *J. Phys. Chem. B* **117**, 4618–4625 (2013).
- Q. Zhang *et al.*, *Adv. Mater.* **29**, 1605506 (2017).
- X. Liu, D. Pan, Y. Hong, W. Guo, *Phys. Rev. Lett.* **112**, 205502 (2014).
- W. Bao *et al.*, *Nat. Nanotechnol.* **4**, 562–566 (2009).
- W. Paszkowicz, J. B. Pelka, M. Knapp, T. Szyszko, S. Podsiadlo, *Appl. Phys. A* **75**, 431–435 (2002).
- D. Lee, P. C. Stevens, S. Q. Zeng, A. J. Hunt, *J. Non-Cryst. Solids* **186**, 285–290 (1995).
- J. W. Wu, W. F. Sung, H. S. Chu, *Int. J. Heat Mass Transfer* **42**, 2211–2217 (1999).
- L. W. Hrubesh, R. W. Pekala, *J. Mater. Res.* **9**, 731–738 (2011).

## ACKNOWLEDGMENTS

We thank C. Jia, Y. Wang, Z. Feng, F. Song, L. Mei, and H. Jing for their help in the laboratory. **Funding:** X.D. is supported by National Science Foundation DMR1508144. Y.H. is supported by National Science Foundation EFR1-1433541. X.X. acknowledges funding from National Natural Science Foundation of China (grants 51602078 and 51878227). H.L. acknowledges funding from National Key Research and Development Program of China (2018YFC0705600). Q.Z. acknowledges funding from Science Fund for Distinguished Young Scholars of Gansu Province (grant 18JR3RA263). C.D. is supported by the Assistant Secretary for Energy Efficiency and Renewable Energy, Building Technologies Program, of the U.S. Department of Energy (contract DEAC02-05CH11231). G.J.C. acknowledges funding from NIST Intelligent Systems Division, NSF (CMMI 1741100), and Office of Naval Research NEPTUNE program. I.S. thanks the Deanship of Scientific Research at King Saud University for its funding of the research through grant PEJP-17-01. X.Z. acknowledges funding from the Office of Naval Research (ONR) MURI program (grant N00014-13-1-0631). **Author contributions:** X.D., Y.H., and H.L. designed and supervised the research; X.X., Q.Z., M.H., and Y.H. conducted experiments with assistance from Z.L., L.P., T.W., X.R., C.Wang, Z.Z., C.Wan, H.F., L.W., J.Z., H.S., B.D., G.J.C., I.S., and X.Z.; M.H. and C.D. conducted the thermal measurement in vacuum; Y.Hu and T.S.F. conducted the thermal measurement in air; Q.Z., W.C., and T.D. conducted the FE and MD simulations; X.X. analyzed the data and prepared the figures. X.D. and X.X. wrote the manuscript with input from all coauthors. All authors reviewed and commented on the manuscript. **Competing interests:** The authors declare no competing interests. **Data and materials availability:** All data are available in the manuscript or the supplementary materials.

## SUPPLEMENTARY MATERIALS

www.sciencemag.org/content/363/6428/723/suppl/DC1  
Materials and Methods  
Supplementary Text  
Figs. S1 to S42  
Table S1  
References (45–62)  
Movies S1 to S4

15 October 2018; accepted 19 December 2018  
10.1126/science.aav7304

## Double-negative-index ceramic aerogels for thermal superinsulation

Xiang Xu, Qiangqiang Zhang, Menglong Hao, Yuan Hu, Zhaoyang Lin, Lele Peng, Tao Wang, Xuexin Ren, Chen Wang, Zipeng Zhao, Chengzhang Wan, Huilong Fei, Lei Wang, Jian Zhu, Hongtao Sun, Wenli Chen, Tao Du, Biwei Deng, Gary J. Cheng, Imran Shakir, Chris Dames, Timothy S. Fisher, Xiang Zhang, Hui Li, Yu Huang and Xiangfeng Duan

*Science* **363** (6428), 723-727.  
DOI: 10.1126/science.aav7304

### Elastic ceramics

Aerogels hold promise as lightweight replacements for thermal insulation. However, poor mechanical stability has hampered progress in moving toward commercialization. Xu *et al.* designed a mechanical metamaterial that pinches in a small amount when you compress it (see the Perspective by Chhowalla and Jariwala). This is characteristic of materials with a negative Poisson's ratio and dramatically improves mechanical stability. The trick was using three-dimensional graphene structures to template the ceramic aerogels, thus producing a superinsulating material endowed with excellent mechanical properties.

*Science*, this issue p. 723; see also p. 694

#### ARTICLE TOOLS

<http://science.sciencemag.org/content/363/6428/723>

#### SUPPLEMENTARY MATERIALS

<http://science.sciencemag.org/content/suppl/2019/02/13/363.6428.723.DC1>

#### RELATED CONTENT

<http://science.sciencemag.org/content/sci/363/6428/694.full>

#### REFERENCES

This article cites 57 articles, 5 of which you can access for free  
<http://science.sciencemag.org/content/363/6428/723#BIBL>

#### PERMISSIONS

<http://www.sciencemag.org/help/reprints-and-permissions>

Use of this article is subject to the [Terms of Service](#)